APL Photonics

RESEARCH ARTICLE | OCTOBER 16 2025

Heterogeneous integration of silicon nitride and amorphous silicon carbide photonics

Zizheng Li ; Bruno Lopez-Rodriguez ; Naresh Sharma ; Roald van der Kolk ; Thomas Scholte ; Harmen Smedes ; R. Tufan Erdogan ; Jin Chang ; Hugo Voncken ; Jun Gao ; Ali W. Elshaari ; Simon Gröblacher ; Iman Esmaeil Zadeh

APL Photonics 10, 106116 (2025)
https://doi.org/10.1063/5.0285619

Heterogeneous integration of silicon nitride and amorphous silicon carbide photonics

Cite as: APL Photon. 10, 106116 (2025); doi: 10.1063/5.0285619
Submitted: 16 June 2025 • Accepted: 3 October 2025 •
Published Online: 16 October 2025

Zizheng Li,[1,a] Bruno Lopez-Rodriguez,[1] Naresh Sharma,[2] Roald van der Kolk,[1] Thomas Scholte,[1] Harmen Smedes,[3] R. Tufan Erdogan,[4] Jin Chang,[3] Hugo Voncken,[1] Jun Gao,[5] Ali W. Elshaari,[5] Simon Gröblacher,[3] and Iman Esmaeil Zadeh[1]

AFFILIATIONS

[1] Department of Imaging Physics (ImPhys), Faculty of Applied Sciences, Delft University of Technology, Delft 2628 CJ, The Netherlands
[2] Department of Electronics Engineering, Indian Institute of Technology (Indian School of Mines), Dhanbad, Jharkhand, India
[3] Department of Quantum Nanoscience, Faculty of Applied Sciences, Delft University of Technology, Delft 2628 CJ, The Netherlands
[4] Department of Precision and Microsystems Engineering, Delft University of Technology, 2628 CD Delft, The Netherlands
[5] Department of Applied Physics, KTH Royal Institute of Technology, Albanova University Centre, Stockholm 106 91, Sweden

[a] **Author to whom correspondence should be addressed:** z.l.li-1@tudelft.nl

ABSTRACT

Amorphous silicon carbide (a-SiC) has emerged as a compelling candidate for applications in integrated photonics, known for its high refractive index, high optical quality, high thermo-optic coefficient, and strong third-order nonlinearities. Furthermore, a-SiC can be easily deposited via CMOS-compatible chemical vapor deposition (CVD) techniques, allowing for precise thickness control and adjustable material properties on arbitrary substrates. Silicon nitride (SiN) is an industrially well-established and well-matured platform, which exhibits ultra-low propagation loss, but it is suboptimal for high-density reconfigurable photonics due to the large minimum bending radius and constrained tunability. In this work, we monolithically combine the a-SiC with SiN photonics, leveraging the merits of both platforms, and achieve the a-SiC/SiN heterogeneous integration with an on-chip interconnection loss of $(0.28^{+0.44}_{-0.28})$ dB and integration density increment exceeding 4444-fold. By implementing active devices on the a-SiC, we achieve 27 times higher thermo-optic tuning efficiency, with respect to the SiN photonic platform. In addition, the a-SiC/SiN platform gives the flexibility to choose the optimal fiber-to-chip coupling strategy depending on the interfacing platform, with efficient side-coupling on SiN and grating-coupling on the a-SiC platform. The proposed a-SiC/SiN photonic platform can foster versatile applications in programmable and quantum photonics, nonlinear optics, and beyond.

I. INTRODUCTION

Photonic integrated circuits (PICs), with the merits including miniaturization, robustness, and high-volume manufacturability, have been one of the cornerstones for applications in data processing, optical communication, and hold potentials in medical imaging, sensing, and quantum computing.[1–6] Various material platforms have been studied and utilized as the foundations for constructing photonic integrated circuits. Among all material platforms which are proposed and researched, silicon (Si) and silicon nitride (SiN) photonics have been the most matured PIC platforms available for mass production in the industry.

Leveraging the micro-electronics fabrication techniques, silicon (Si) photonics has flourished over the past decades.[7] Si's high refractive index and large thermo-optics coefficient enable high integration density and low-power tunable photonic devices.[8–10] However, the presence of two-photon absorption in silicon hinders silicon photonics from scaling up to very large photonic networks, so that prevents the realization of more advanced applications.[11,12] Silicon's relatively narrow energy bandgap (~1.1 eV) also results

in high absorption losses at visible wavelengths, limiting silicon photonics to, mostly, the telecommunication wavelengths.[13,14] Silicon nitride (SiN), on the other hand, provides ultra-low waveguide propagation losses in a wide transparency window covering both the visible and telecommunication wavelengths, thereby facilitating versatile photonic devices and applications.[15–18] In addition, SiN offers a relatively large Kerr coefficient.[19,20] These characteristics together make SiN an excellent host for nonlinear optics applications, including wavelength conversion, entanglement generation, frequency combs, and more.[16,20–28] To realize the ultra-low loss SiN waveguides, high-aspect-ratio waveguides (width:height > 10:1) have been proposed and successfully fabricated using either the subtractive or Damascene processes, where the optical modes are weakly confined around the waveguide slab to exploit the low-absorption advantage of silicon dioxide (SiO_2) cladding. To fabricate such ultra-low loss SiN waveguides, high-temperature (≥1200 °C) annealing and chemical–mechanical polishing (CMP) are essential to effectively minimize the loss.[15,16,29–31] Owing to the SiN's relatively low refractive index, large minimal bending radius (on the millimeter to sub-centimeter scale) is necessary, which compromises the integration density. In addition, to prevent metal absorption loss, the high-aspect ratio SiN platform requires a sufficiently thick cladding layer on top of the waveguides (6–15 μm) that separates the SiN waveguides from the micro-heaters when employing thermo-optic tuning; this hampers the SiN photonics from pursuing efficient tunability and poses challenges in thermal crosstalk control. Combined with the low intrinsic thermo-optic coefficient of SiN, it is challenging to achieve an efficient thermo-optic tuning on high-aspect-ratio SiN planform.[32–34] Therefore, despite the prevalence and maturity of Si and SiN photonics, their performance ceiling in scaling-up and effective tuning has driven the demand of investigating new photonic platforms.

Amorphous silicon carbide (a-SiC) is a promising photonic platform that emerged recently, appealing for its properties involving large and tunable bandgap (~2.5 eV), relatively high and tunable refractive index (~2.4–2.9 at 1550 nm), low loss (0.78 dB/cm), large thermo-optic coefficient (1.12×10^{-4}/°C), and large Kerr-nonlinear coefficient (6.7×10^{-18} m^2/W).[35–41] However, despite the advancements achieved in the recent literature, the a-SiC exhibits higher optical loss compared to SiN. Heterogeneous integration of a-SiC on lithium niobate via low-temperature chemical vapor deposition (CVD) deposition has been recently realized, showing that a-SiC's low-temperature fabrication techniques are compatible with the different substrates, with precise thickness control, and excellent surface roughness without polishing.[42]

In various PIC platforms, fiber-to-chip interfacing has remained a persistent topic in integrated photonics research. Side-coupling (or edge-coupling), which is known for its high coupling efficiency and large bandwidth, has been extensively studied by researchers over the decades since the origin of integrated photonics.[43–49] The primary challenge of side-coupling is the substantial mode mismatch between the modes in optical fibers and photonic waveguides. Delicate design and fabrication are needed to realize the adiabatic transition from the strongly confined waveguide modes into weakly confined modes that match that of the fiber modes. Grating-coupling is another widely adopted fiber-to-chip coupling strategy, which obviates the need for chip-facet exposure and additional waveguide routing, thereby simplifies the fabrication process. It also outperforms in alignment tolerance, compared to edge-coupling. These facts make grating-coupling inherently compatible with wafer-scale production and characterization. Designing high-coupling-efficiency grating couplers requires an optimal grating period and favors a large film thickness and high refractive index contrast.[48,50–54] With above arguments, the high-aspect-ratio SiN waveguide, the record-low propagation loss holder, is unsuitable for achieving high-efficiency grating-coupling. On the other hand, in high refractive index material platforms, such as a-SiC, it is challenging to realize efficient edge-coupling. This is not the case when the roles are reversed; each platform becomes well-suited for the other's task. For instance, the high-aspect-ratio SiN's weak confinement leads to a large mode area, and makes the mode matching easier, while a-SiC's high refractive index offers more design flexibility for grating couplers. The proposed a-SiC/SiN heterogeneous integration provides a unified solution for fiber-to-chip interfacing, enabling both grating-coupling and edge-coupling to be employed optimally.

Thermo-optic tuning is widely exploited to actively control the on-chip photonic devices in large-scale PICs for photonic computing and quantum computing.[4,6,55–63] Thermal tuning efficiency and power consumption are recognized as the pivotal performance benchmarks of a PIC, meanwhile the scalability is also highly valued, which is mainly limited by waveguide losses. The a-SiC/SiN heterogeneous photonic platform leverages the high thermal optical coefficient of amorphous silicon carbide, empowering the ultra-low loss high-aspect-ratio SiN photonics with efficient thermo-optic tunability; together they present an effective and technically feasible approach toward a scalable, densely integrated, ultra-low loss, and highly tunable photonic platform.

In this paper, we propose a heterogeneous a-SiC/SiN photonic integrated circuit that combines the high-aspect-ratio SiN waveguides with efficiently thermo-optic tunable and high integration density a-SiC waveguides. By showcasing the key building blocks, including low-loss a-SiC/SiN interconnection couplers and fiber-to-chip grating couplers, we outline the potential directions for future applications enabled by this platform, taking advantages of its ultra-low loss, wide transparency window, high integration density, efficient thermo-optic tunability, and strong third-order nonlinearity properties.

II. PHOTONIC DEVICES AND PERFORMANCE CHARACTERIZATION

Two different setups, one for side-coupling and the other for grating-coupling, are employed to characterize the performance metrics of the a-SiC/SiN platform, including the thermal optics response, a-SiC/SiN interconnection coupling, edge-coupling, and grating-coupling. Figures 1(a), 1(b), and S1 in the supplementary material show the corresponding setups. The characterization is performed with tunable lasers (Photonetics TUNICS-PRI 3642 HE 15 and Keysight 81940A). The light is sent to the photonic chip via a single-mode fiber, passing through a paddle polarization controller (FPC560). The output light is collected by a multi-mode fiber and delivered to an optical powermeter (Newport 818-NR) or photoreceiver (Newport 1811 New Focus). For grating-coupling, the fibers are positioned at an angle of 10° relative to the normal of the sample. For side-coupling, we use translation stages to align optical fibers

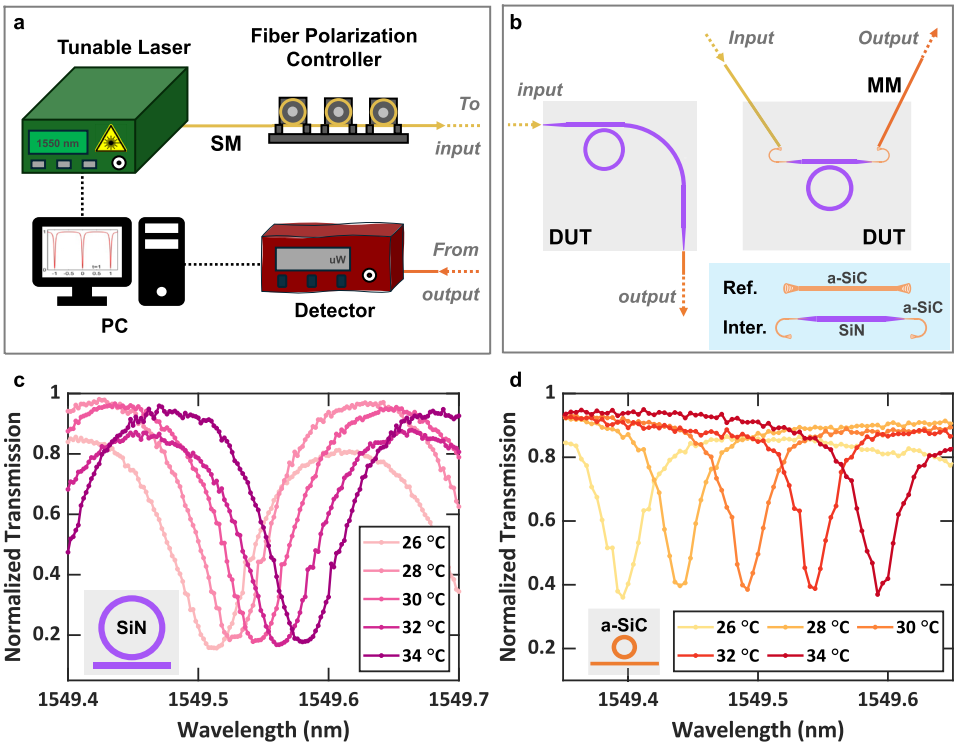

FIG. 1. (a) Characterization setups used to measure the on-chip devices. (b) Two kinds of fiber-to-chip accesses employed in measurements. The blue-background inset illustrates both the interconnection device and the corresponding reference device employed for characterization. [(c) and (d)] Thermo-optic characterization of the a-SiC/SiN platform: the resonance shifts observed when sweeping the temperature from 26 to 34 °C on the SiN ring resonator and a-SiC ring resonator, respectively.

to the exposed waveguide cross sections. To measure the thermo-optics response, the sample is mounted and pasted on the sample stage, using thermally conductive silver paste. Heat is applied to the sample stage by a proportion–integration–differentiation temperature controller to globally adjust the temperature of the whole chip. A temperature sensor in the stage provides feedback to the temperature controller to maintain a stable temperature. To characterize the interconnection coupling efficiency, we designed and fabricated the devices shown in the inset of Fig. 1(b), highlighted with a blue background. The interconnection devices (Inter.) consist of two grating couplers as input and output and two interconnection couplers connecting the a-SiC and SiN waveguides, while the reference devices (Ref.) are made of two grating couplers connected by a straight a-SiC waveguide. The fabrication details are presented in Sec. II in the supplementary material. The definitions of the characterized performance metrics are discussed in detail in Sec. III.

A. Thermal optics

On-chip tunability after fabrication is vital for all applications that require programmability and reconfigurability. As a key feature of the proposed a-SiC/SiN platform, the thermo-optic tunability is characterized utilizing the on-chip ring resonators. We apply global heating to the a-SiC/SiN sample and monitor the resonance wavelength shift with respect to the temperature variation, using the characterization setup shown in Figs. 1(a) and 1(b). On the same sample, a-SiC microrings with a bending radius of 120 μm and SiN microrings with a bending radius of 1100 μm are fabricated and measured. The a-SiC rings demonstrate a 25.0 pm/°C shift over the temperature change from 26 to 34 °C, whereas the measured SiN ring spectra show a 8.6 pm/°C temperature shift over the same range, as illustrated in Figs. 1(c) and 1(d). Considering that the SiN ring resonators possess a much larger bending radius, hence a much larger heating area, we normalize the thermo-optic shift to the unit ring-waveguide length and take it as the metric to evaluate thermo-optic tunability. According to the measured results, the a-SiC ring shows a thermo-optic tunability of 33.2×10^{-3} pm/°C/μm, while the SiN ring shows 1.2×10^{-3} pm/°C/μm. It is concluded that a-SiC has 27 times stronger thermo-optic tunability compared to SiN. A thermo-optic coefficient of 5.1×10^{-5}/°C for a-SiC, and 3.6×10^{-5}/°C for SiN, are extracted (details in Sec. III), showing good agreement with the recent studies.[10,36,64] The heterogeneous integration of the a-SiC and SiN opens the way for ultra-low-loss SiN photonics to attain efficient tunability while providing highly programmable a-SiC photonics with low-loss delay lines, among other possible advanced functionalities.

B. a-SiC/SiN interconnection couplers

A key feature of this heterogeneous platform is the loss associated with the transitions between the a-SiC and SiN layers. In this section, we present the a-SiC/SiN interconnection couplers, which serve as the bridge enabling bidirectional light coupling between the a-SiC and SiN layers. The structure of the interconnection coupler is shown in Fig. 2(a). It adiabatically converts the mode propagating in the a-SiC waveguides into the mode supported by SiN waveguides, and vice versa. The design principle of such devices is described in our previous studies.[65,66] The ultra-low loss SiN platform relies on the high aspect ratio waveguides, where a greater aspect ratio is proven to provide lower loss.[31] At telecom wavelengths, the

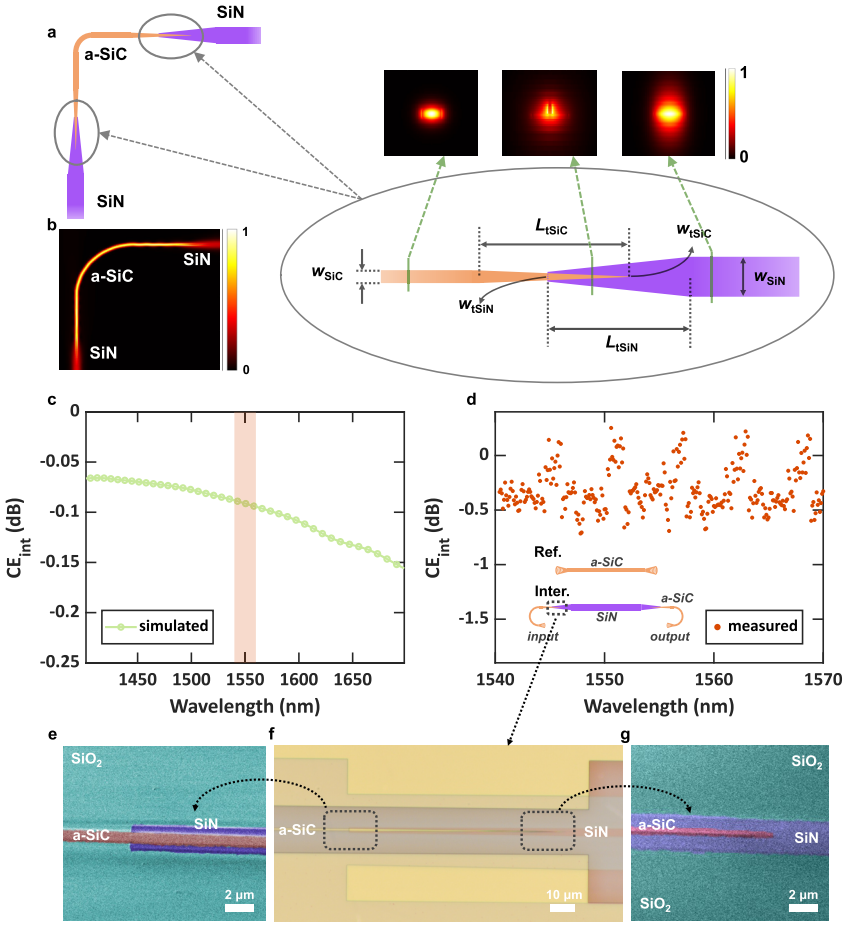

FIG. 2. (a) Schematic illustration of the a-SiC/SiN interconnection coupler, with a zoomed-in figure showing the interconnection coupling region. The three insets are the simulated mode profiles in the a-SiC waveguide, at the coupling region, and in the SiN waveguide. (b) Simulated electric field intensity distribution of the light propagating between the SiN and a-SiC layers, through the a-SiC 90° bending and interconnection couplers. (c) Simulated interconnection coupling efficiency, with a light-orange strip showing the wavelength range of experimental measurements. (d) Measured interconnection coupling efficiency. The insets depict the fabricated reference device (Ref.) and interconnection coupler (Inter.). (e) Scanning electron microscopy image of the SiN tip in the interconnection coupler. (f) Optical microscopy image of the interconnection coupler. (g) Scanning electron microscopy image of the a-SiC tip in the interconnection coupler.

dimensions of single mode waveguides are 100 nm × 3 μm. In contrast, the a-SiC single mode waveguide has a size of 260 × 800 nm^2.[35] The refractive index contrast between a-SiC and SiN, reaching Δn = 0.6 around 1550 nm, along with the 160 nm thickness difference of a-SiC/SiN waveguides, results in a significant mode mismatch. To overcome this mismatch and achieve phase matching, both the a-SiC and SiN waveguides are adiabatically tapered down to the final tip widths. The widths of the a-SiC and SiN waveguides are represented as w_{SiC} and w_{SiN}, respectively, in Fig. 2(a) inset. As shown in the zoomed-in illustration, the a-SiC and SiN waveguides are tapered toward the center of the device, with their widths decreasing to the final tip widths of w_{tSiC} and w_{tSiN}, respectively.

The tapering lengths are denoted as L_{tSiC} and L_{tSiN}. We use finite-difference-eigenmode method to calculate the optical mode profiles and finite-difference time-domain (FDTD) method to simulate light propagation in the a-SiC/SiN interconnection coupler. The mode profiles of the light propagating in the a-SiC waveguide, the a-SiC/SiN coupling region, and the SiN waveguide are shown in the three insets at the top right, from left to right, respectively. We introduce a 90° turn to determine and verify the minimal bending radius of a-SiC, and found a minimal bending radius smaller than 10 μm. The electric-field intensity distribution in the device, in which light launched into a SiN waveguide is coupled to an a-SiC waveguide, guided through a 90° bend, and subsequently coupled back to another SiN waveguide, is shown in Fig. 2(b). The coupling efficiency of the a-SiC/SiN interconnection coupler, CE_{int}, is simulated by the FDTD method (Ansys Lumerical) as shown in Fig. 2(c), with a light orange strip highlighting the wavelength range that is experimentally investigated. The standard single-mode a-SiC and SiN waveguides have widths of 0.8 and 3 μm, respectively. The optimal taper tip widths are w_{tSiC} = 50 nm and w_{SiN} = 2 μm, according to the simulations. The results exhibit that the interconnection loss is less than 0.1 dB per connection at 1550 nm.

Experimentally, we characterized the bending losses of the a-SiC waveguides by measuring the intrinsic quality factors of the ring resonators with different bending radii, and discovered that the minimal bending radius can be smaller than 15 μm (see Sec. IV in the supplementary material). We believe that the minimal bending radius can be reduced to below 10 μm by optimizing the single mode waveguide geometry. As comparison, the minimal bending radius for the 100 nm thick high-aspect ratio SiN waveguide is larger than 1 mm.[31] This indicates that combining the a-SiC/SiN photonics on the same chip enables compact photonic routing and smaller device footprint, hence significantly increases the integration density, which is essential for scalable PIC design. Considering the photonic devices (for example, ring resonators, spirals, and

routing bends) scale with the square of the minimal bending radius R^2, the integration density ρ can be evaluated as $\rho \propto 1/R^2$. The experimental results reveal a 4444-fold integration density difference between the a-SiC/SiN photonics and SiN photonics. Regarding the a-SiC/SiN interconnection coupling, as shown in Fig. 2(d), a coupling loss of $(0.28^{+0.44}_{-0.28})$ dB per a-SiC/SiN connection is measured from the devices with the optimal parameters suggested by the simulation results. The results are obtained via normalizing the averaged output power from four identical interconnection couplers to the output power of the reference devices (detailed in Sec. III, with the statistical treatment explained in Sec. III in the supplementary material). The oscillations superimposed on the signal stem from the grating-to-grating reflections within the interconnection (Inter.) and reference (Ref.) devices, where the a-SiC and SiN waveguides form Fabry–Perot cavities between the gratings. Figure 2(f) shows the optical microscope image of the fabricated a-SiC/SiN interconnection coupler, while the a-SiC and SiN taper end tips are inspected using a scanning electron microscope, as shown in Figs. 2(e) and 2(g), respectively.

To further study the fabrication tolerance, we sweep the parameters of the a-SiC tip width w_{tSiC} from 30 to 70 nm and SiN tip width w_{tSiN} from 1.4 to 2.4 μm. The measurement results are displayed in Fig. S3 in the supplementary material. For each of the parametric sweeps, five devices are fabricated on the same sample.

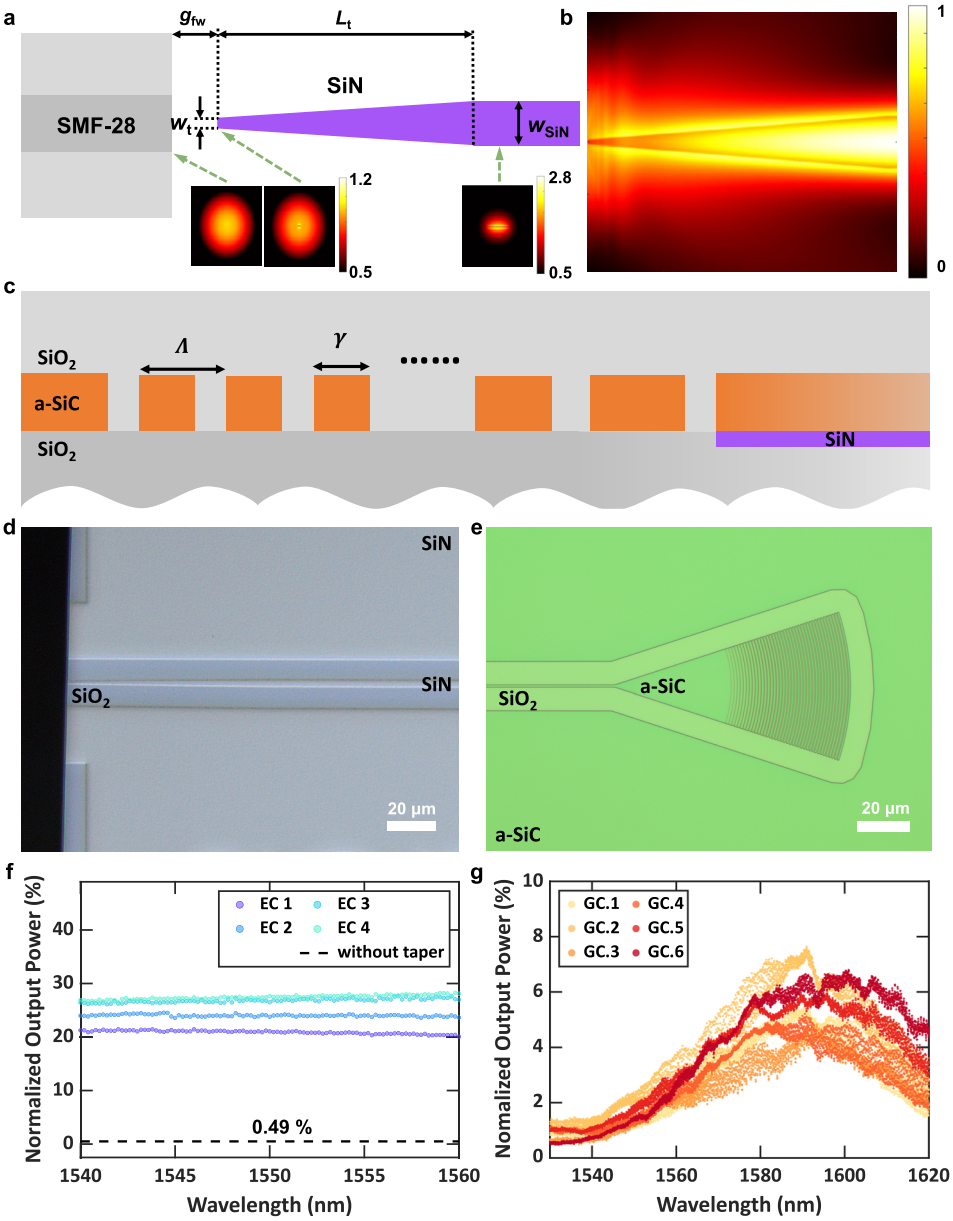

FIG. 3. (a) Schematic showing the fiber-to-chip coupling using inverted taper edge coupler, with taper end tip width w_t and taper length L_t. g_{fw} represents the fiber-to-waveguide gap. (b) Simulated electric field intensity distribution in the edge coupling process. (c) Schematic of the apodization grating coupler, with grating period Λ and grating width γ. (d) Optical microscopy image showing the fabricated edge coupler. (e) Optical microscopy image showing the fabricated grating coupler. (f) Measured power from devices' output, after passing through the input edge coupler (EC), 90° waveguide bend, and the output edge coupler, which is normalized to laser power. On the same chip, four identical devices with the optimized parameters are measured. The dashed line shows the coupling of the standard single-mode waveguides without inverted tapers. (g) Measured output power, after passing through two grating couplers (GCs) connected by a straight waveguide, which is normalized to the laser power.

The sweeping results of w_{tSiC} and w_{tSiN} show a maximum extra loss of 1.1 dB in CE_{int}. The change in the a-SiC tip width w_{tSiC} results in a more significant impact on CE_{int}. In general, the a-SiC/SiN exhibits good fabrication tolerances. The same design protocol can also be applied to the a-SiC/SiN integration platform with other layer thicknesses, for SiN waveguides with different aspect ratios and applications in a variety of wavelengths. We additionally conducted an investigation to validate that the SiN photonics loss remains unaffected after the co-integration with the a-SiC, as discussed in Sec. VI of the supplementary material.

C. Edge couplers

One of the most commonly used fiber-to-chip coupling method is edge-coupling (or side-coupling), which provides a higher coupling efficiency and wider bandwidth compared to grating couplers. To overcome the prominent challenge of mode mismatch between the single-mode fiber and the optical waveguide, we design and optimize an inverted taper mode converter. At the wavelength of 1550 nm, the mode area in the standard SMF-28 single-mode fiber is roughly 75.1 μm^2; by contrast, the mode area in the a-SiC single-mode waveguide is 0.4 μm^2, while in the high aspect ratio SiN waveguide, it is 4.1 μm^2. The high width-to-height ratio can be leveraged to further promote the weak-confinement feature by tapering down the waveguide width, thereby enlarging the waveguide mode area and mitigating the mode mismatch between the fiber and waveguide. As shown in Fig. 3(a), the SiN waveguide is tapered down to the optimal tip width w_t = 570 nm, where the best mode matching and the highest mode overlapping are realized, indicating a theoretical coupling efficiency up to 91.9% per fiber-to-chip interface when the fiber-to-waveguide gap is zero (g_{fw} = 0). The simulated power distribution of the fiber-to-chip coupling process is shown in Fig. 3(b).

To experimentally investigate the performance of the designed edge couplers, we fabricate four identical devices, each consisting of two edge couplers connected by a 90° waveguide bend. The sample is cleaved twice perpendicularly to expose the cross sections of the edge couplers. The measurement is done using a single-mode fiber as an input injecting light to one of the edge couplers and a multi-mode fiber collecting from the output, as shown in Figs. 1(a) and 1(b). The measured output power, normalized to the laser, is presented in Fig. 3(f). Two devices consisting of cleaved standard SiN single-mode waveguides connected by a 90° bend, without tapered edge couplers, are taken as a reference. The measured results are averaged and represented by the black dashed line in Fig. 3(f). The measured results show that up to 27.45%, the power of the input can be collected at the output, after experiencing two fiber-to-chip interfaces. In comparison, without the taper only 0.49%, the power is collected at the output, indicating a 55-fold improvement in coupling efficiency with the inverted taper structure. The details of the characterization and analysis are provided in Sec. III. More microscopy pictures demonstrating the sample edges after cleaving are included in Sec. V in the supplementary material, along with a simulation analysis on how the fiber-to-chip air gap and fiber misalignment are influencing the coupling efficiency.

D. Grating couplers

The other commonly used component to realize the fiber-to-chip coupling is grating couplers, which excel in alignment tolerance and convenient fiber-to-chip access and are well-suited for multi-input and multi-output reconfigurable photonics. Automated wafer-scale characterization of large device arrays also benefits from this approach. We calculated the grating period based on the Bragg Condition,[67] $\Lambda = \lambda/(n_{eff} - n_{clad} \cdot \sin\theta)$, where Λ is the grating period, λ is the working wavelength, n_{eff} and n_{clad} represent the effective index of the desired waveguide mode and refractive index of the cladding, respectively, and θ denotes the fiber angle with respect to the sample norm. Considering the fundamental TE mode supported by the a-SiC waveguides, a grating period of Λ = 1002 nm is calculated for the 10° fiber angle. In the grating coupler design, we keep the first 20 periods (away from the straight waveguide) uniform with the calculated period Λ, while the subsequent 20 periods with apodization linewidths γ_0 to γ_{20} (from the device edge to the grating center), as depicted in Fig. 3(c). Using the setup demonstrated in Figs. 1 and S1(a), the laser light is coupled to the a-SiC waveguide through a SMF-28 single-mode fiber, and a multi-mode fiber is employed to collect the output from another grating coupler. We measured six fabricated grating coupling devices [Ref. configuration as shown in Fig. 1(b)] with the grating linewidth apodized from γ_0 = 600 nm to γ_{20} = 940 nm for GC.1 to 3, and γ_0 = 720 nm to γ_{20} = 960 nm for GC.4 to 6; the results are shown in Fig. 3(g). A maximum normalized output power of 7.7% is achieved at 1590 nm, while the values exceeding 2.4% are measured around 1550 nm. The oscillations superimposed on the signal are attributed to the Fabry–Perot cavity formed by grating-to-grating reflections. The detailed definition of the coupling efficiency can be found in Sec. III.

III. METHOD

To characterize the thermo-optic coefficients of the a-SiC and SiN photonics, we use the methods introduced in the literature.[33,35,64,68] The following equation relates the effective index change along temperature change with the material thermo-optic coefficients by

$$\begin{aligned} \frac{dn_{eff}}{dT} &= \Gamma_{SiO_2}\frac{dn_{SiO_2}}{dT} + \Gamma_{a-SiC}\frac{dn_{a-SiC}}{dT}, \\ \frac{dn_{eff}}{dT} &= \Gamma_{SiO_2}\frac{dn_{SiO_2}}{dT} + \Gamma_{SiN}\frac{dn_{SiN}}{dT}, \end{aligned} \tag{1}$$

where Γ denotes the mode overlap integral in the corresponding material, which is obtained from finite difference eigenmode simulations, and the thermo-optic coefficient of SiO_2 is $0.96 \times 10^{-6}/°C$, as determined in the literature.[33] The effective index change of the fundamental waveguide mode can be obtained from the measured resonance wavelength shift, given by the following equation:

$$\frac{d\lambda}{dT} = \left(n_{eff} \cdot \alpha_{sub} + \frac{dn_{eff}}{dT}\right) \cdot \frac{\lambda}{n_g}, \tag{2}$$

where $\alpha_{sub} = 2.6 \times 10^{-6}/°C$ is the thermal expansion coefficient of the substrate.

The a-SiC/SiN interconnection coupler efficiency is obtained based on the averaged measurement results that were obtained from multiple identical devices. Assuming that the two interconnection couplers within the same device hold identical optical responses, the interconnection coupling efficiency CE_{int} can be defined in the following equation:

$$P_{\text{out}} = P_{\text{in}} \cdot CE_{\text{gc-in}} \cdot \alpha_{\text{a-SiC}} \cdot \alpha_{\text{SiN}} \cdot CE_{\text{int}}^2 \cdot CE_{\text{gc-out}}\,, \tag{3}$$

while the reference device can be expressed by

$$P'_{\text{out}} = P_{\text{in}} \cdot CE_{\text{gc-in}} \cdot \alpha'_{\text{a-SiC}} \cdot CE_{\text{gc-out}}. \tag{4}$$

In Eqs. (3) and (4), P_{in}, P_{out}, and P'_{out} denote the input power, the output power from Inter. devices, and the output power from Ref. devices, respectively. The measured raw data of P_{out} and P'_{out}, along with the statistics treatment details supporting the results in Fig. 2(d), can be found in Sec. III in the supplementary material. $\alpha_{\text{a-SiC}}$ and α_{SiN} represent the losses in the a-SiC and SiN waveguides, respectively, in the interconnection coupler. $CE_{\text{gc-in}}$ and $CE_{\text{gc-out}}$ are the coupling efficiencies of the input and output a-SiC grating couplers, respectively. Assuming that on the same sample the grating couplers have the same response, the a-SiC/SiN interconnection coupler coupling efficiency can be written as the following equation:

$$CE_{\text{int}} = \sqrt{\frac{P_{\text{out}}}{P_{\text{in}} \cdot \alpha_{\text{a-SiC}} \cdot \alpha_{\text{SiN}} \cdot CE_{\text{gc-in}} \cdot CE_{\text{gc-out}}}} = \sqrt{\frac{P_{\text{out}} \cdot \alpha'_{\text{a-SiC}}}{\alpha_{\text{a-SiC}} \cdot \alpha_{\text{SiN}} \cdot P'_{out}}}. \tag{5}$$

Regarding grating-coupling, devices with two grating couplers connected by an a-SiC waveguide are fabricated, where the light coupling process is expressed as

$$P_{\text{gc-out}} = P_{\text{in}} \cdot CE_{\text{gc-in}} \cdot \alpha_{\text{gc-SiC}} \cdot CE_{\text{gc-out}}\,, \tag{6}$$

where $\alpha_{\text{gc-SiC}}$ is the loss generated by the connecting a-SiC waveguide. The normalized output power is used to quantify the grating-coupling efficiency,

$$P_{\text{gc-norm}} = \frac{P_{\text{gc-out}}}{P_{\text{in}} \cdot \alpha_{\text{gc-SiC}}}\,. \tag{7}$$

For edge coupling efficiency measurement, the devices that consist of a L long SiN waveguide and two edge couplers are fabricated. The light coupling can be expressed as

$$P_{\text{sc-out}} = P_{\text{in}} \cdot CE_{\text{sc-in}} \cdot \alpha_{\text{sc-SiN}} \cdot CE_{\text{sc-out}}\,, \tag{8}$$

where $\alpha_{\text{sc-SiN}}$ is the loss generated by the connecting SiN waveguide and $CE_{\text{sc-in}}$ and $CE_{\text{sc-out}}$ represent the input and output side-coupling efficiencies, respectively. The normalized output power used for quantifying the side-coupling efficiency is defined as

$$P_{\text{sc-norm}} = \frac{P_{\text{sc-out}}}{P_{\text{in}} \cdot \alpha_{\text{sc-SiN}}}\,. \tag{9}$$

The waveguide losses are characterized by the intrinsic quality factors of the ring resonators fabricated on the a-SiC layer and SiN layer on the same sample. We translate the intrinsic quality factor Q_{i} into propagation loss α, in the unit of dB/cm, as expressed below:

$$Q_{\text{i}} = \frac{2Q_{\text{L}}}{1+\sqrt{T}} = \frac{2\lambda_0}{FWHM(1+\sqrt{T})}, \tag{10}$$

$$\alpha\ (\text{dB/m}) = 4.3429 \cdot \alpha(\text{m}^{-1}) = 4.3429 \cdot \left(\frac{2\pi n_g}{Q_i \lambda_0}\right), \tag{11}$$

where λ_0 denotes the center wavelength, the full-width half-maximum (FWHM) of the resonance dips and the on resonance transmission T are measured experimentally, and n_{g} is the group index of the propagation mode, obtained from the free spectral range (FSR) of the ring resonator,

$$n_{\text{g}} = \frac{\lambda^2}{2\pi R \cdot FSR}. \tag{12}$$

IV. PROSPECTS OF a-SiC/SiN PLATFORM FOR FUTURE APPLICATIONS

In large-scale reconfigurable PICs, thermo-optic phase shifters employed with micro-heaters are the key building blocks. The thermo-optic tuning efficiency and thermal crosstalk are the most critical performance metrics when scaling up to increasingly complex networks. We analyze the trade-off between maximizing the thermal-optic tuning efficiency and minimizing the metal absorption loss on our a-SiC/SiN heterogeneous platform. As shown in Fig. 4(a), the strong confinement of the a-SiC allows for a minimum heater–waveguide gap of 600 nm, while for SiN, the gap has to be larger than 5 μm to prevent additional absorption. We simulate the heat (temperature) distribution when the titanium nitride (TiN) heaters are set to 350 K, as shown in the insets. Temperature contours for 305, 315, 325, and 335 K are plotted in figures. A clear temperature difference is observed around the a-SiC and SiN waveguides when the TiN heaters on top are set to the same temperature that the a-SiC waveguide reaches ~320 K, while the SiN waveguide receives nearly-zero heat. This pronounced difference arises from the disparity in optical confinement strength between SiN and a-SiC and the bad thermal conductivity of the SiO_2 cladding. Together with the huge thermo-optic coefficient contrast discussed in Sec. II A, the a-SiC photonics exhibit markedly superior thermo-optic performance over the SiN photonics. This highlights the advantage of the co-integration, where tunable devices are implemented compactly and densely in the a-SiC layer with high tuning efficiency, while the SiN layer is dedicated to low-loss propagation.

Examples of the future applications of the proposed heterogeneous a-SiC/SiN PIC are depicted in Fig. 4(b), where we mark the a-SiC in orange, SiN in dark blue, TiN in yellow, SiO_2 in black, and Si substrate in red. The optical fibers (in green) are positioned either toward the exposed sample facets for edge-coupling or angled at 20° from above for grating-coupling. Employing the pick-and-place technique, we foresee the immediate implementation of deterministic integration of nanowire quantum dots (NW-QDs) as single photon emitters and subsequently quantum optics experiments on the a-SiC/SiN platform.[69–73] Devices delay lines with tens of nanoseconds delayed time with the distinctive advantage of combining the high density and high tunability a-SiC photonics with ultra-low-loss SiN photonics; the a-SiC/SiN photonic platform can emerge as a compelling choice for scalable and reconfigurable photonics. The figure is not to scale, and the minimum bending radii for the SiN and a-SiC photonics are 1000 and 15 μm, respectively.

Table I lists the comparison of the key performance metrics of different tunable PIC platforms, including integration density ($\rho = 1/R_{\text{min}}^2$), waveguide loss, thermo-optic coefficient, power consumption for π phase shift, and fabrication cost per minimal device

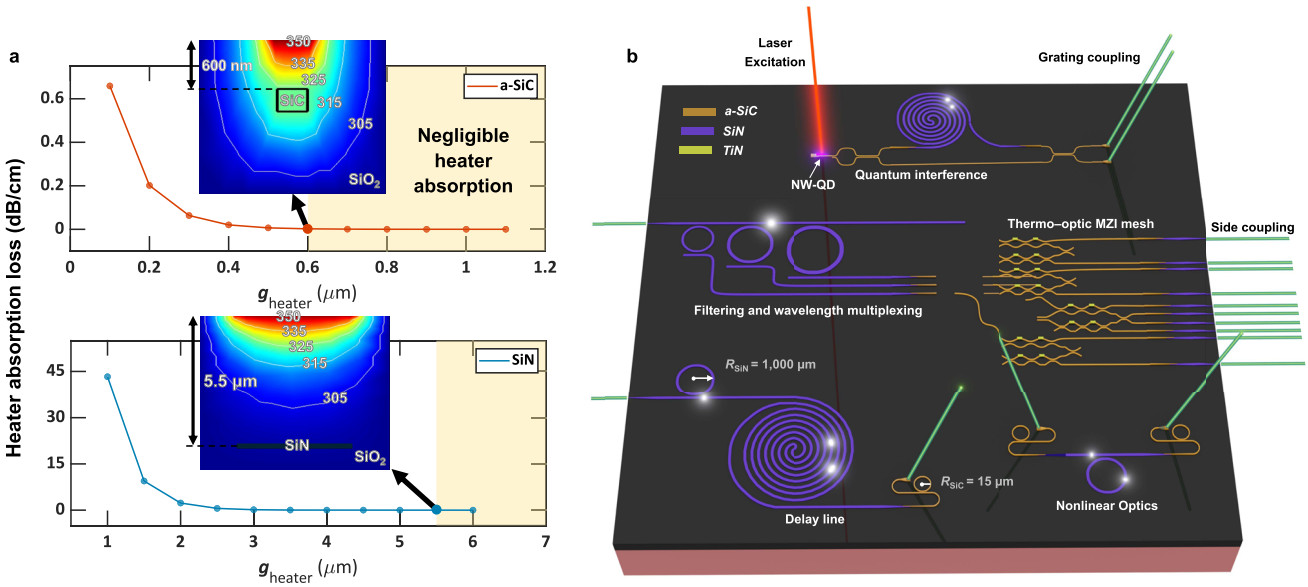

FIG. 4. (a) Simulation analysis of the TiN heater absorption losses with respect to the heater–waveguide gap for the a-SiC waveguides (upper panel) and SiN waveguides (lower panel). The light-yellow shaded area marks the regime where the metal absorption losses are negligible. The insets illustrate the heat (temperature) distribution when the TiN heaters are set to the same temperature of 350 K. (b) Illustration of the a-SiC/SiN heterogeneous photonic integrated circuit with the functional devices and potential applications. The glowing white dots illustrate the photons propagating in the waveguides. The optical fibers are represented using green color, and the free-space laser beam is depicted with red color.

TABLE I. Comparison of the key performance metrics between a large-scale a-SiC/SiN photonic network and other material platforms.

Platform[a]	Integration density (/mm^2)[b]	Waveguide loss (dB/cm)	Thermo-optic coefficient (/°C)	Power consumption per π phase shift (mW)	Fabrication price per minimal device area ($ mm^2)[c]	References
a-SiC/SiN	4444	0.001–0.78	5.1×10^{-5}	35	0.229	This work, 15, and 35
Si	40 000	1.5–4	1.8×10^{-4}	20	0.013	74–76
SiN (M)	100	0.15–1.5	2.5×10^{-5}	88	5.080	77–82
SiN (H)	1	0.001–0.1	2.5×10^{-5}	300	614.644	15, 17, 69, and 83–85

[a]Standard 220 nm silicon on the insulator platform, SiN moderate confinement (SiN–M) platform with a waveguide thickness of 300–400 nm, and SiN high-aspect-ratio (SiN–H) platform with waveguide thickness ≤100 nm, at the wavelength of 1550 nm. The a-SiC/SiN platform proposed in this work combines the 260 nm a-SiC photonics with the 100 nm high-aspect-ratio SiN.
[b]Defined as $\rho = 1/R_{min}^2$, where R_{min} denotes the minimal bending radius of the platform.
[c]The method used to estimate prices is detailed in the supplementary material.

area. Here, we use the square of the minimal bending radius (R_{min}^2) to represent the minimal device area. In the table, we focus on single-mode waveguides at telecom wavelengths; therefore, strongly confined (thick-film) platforms are excluded from comparison. More detailed sources of these estimations are provided in Sec. VII in the supplementary material. As presented in the table, the Si PIC offers the highest integration density and thermo-optic tunability, albeit at the cost of high waveguide loss. The SiN PIC platforms, namely the moderate confinement and high-aspect-ratio SiN, exhibit low waveguide loss but suffer from high fabrication expense and thermal tuning power consumption. In comparison, the a-SiC/SiN PIC possesses high integration density and efficient thermal tunability that are comparable to the Si PIC, while it retains the low-loss characteristic of the high-aspect-ratio SiN PIC. Owing to the substantial difference in integration densities, the heterogeneous a-SiC/SiN platform also shows a notable advantage in fabrication price per minimal device area (R_{min}^2).

V. CONCLUSION

This work presents the design and experimental demonstration of the heterogeneous photonic integrated a-SiC/SiN platform. The proposed solution combines the merits of both a-SiC and SiN photonics, while circumventing their respective shortcomings. With the a-SiC/SiN platform, we demonstrate a feasible path for leveraging the ultra-low optical loss and wide transparent window of the SiN photonics, meanwhile featuring up to 4444 times higher integration density and 27 times higher thermo-optic tuning efficiency in terms of per unit waveguide length, enabled by the a-SiC photonics. The most important element of this heterogeneous platform,

the a-SiC/SiN interconnection coupler, has been demonstrated to enable efficient interconnections between the a-SiC and SiN photonics, with a coupling loss of $(0.28^{+0.44}_{-0.28})$ dB. Both grating-coupling and side-coupling can be achieved on the same chip, which provides more fiber-to-chip interfacing freedom for distinct requirements from versatile applications. Furthermore, the platform combines two materials that possess high Kerr nonlinear coefficients, which provides the potential of efficient four wave mixing and the realization of the on-chip single photon sources. The realization of this heterogeneous a-SiC/SiN platform stands as a compelling candidate toward more advanced applications in integrated photonics, quantum photonics, and beyond.

SUPPLEMENTARY MATERIAL

The supporting information can be found in the supplementary material.

ACKNOWLEDGMENTS

The authors acknowledge the help and valuable advices from Thim Zuidwijk, Charles de Boer, and Hozanna Miro. Z.L. acknowledges the China Scholarship Council (CSC, 202206460012). N.S. and I.E.Z. acknowledge the funding from the NWO OTP COMB-O project (Project No. 18757). I.E.Z. acknowledges funding from the European Union's Horizon Europe research and the innovation program under Grant Agreement Nos. 101098717 (RESPITE project) and 101099291 (fastMOT project).

AUTHOR DECLARATIONS

Conflict of Interest

The authors have no conflicts to disclose.

Author Contributions

Zizheng Li and Bruno Lopez-Rodriguez contributed equally to this work.

Zizheng Li: Conceptualization (equal); Data curation (equal); Formal analysis (equal); Investigation (equal); Methodology (equal); Project administration (equal); Resources (equal); Software (equal); Supervision (equal); Validation (equal); Visualization (equal); Writing – original draft (equal); Writing – review & editing (equal). **Bruno Lopez-Rodriguez**: Conceptualization (equal); Data curation (equal); Formal analysis (equal); Investigation (equal); Methodology (equal); Project administration (equal); Resources (equal); Software (equal); Supervision (equal); Validation (equal); Writing – review & editing (equal). **Naresh Sharma**: Conceptualization (equal); Data curation (equal); Formal analysis (equal); Investigation (equal); Methodology (equal); Project administration (equal); Software (equal); Supervision (equal); Writing – review & editing (equal). **Roald van der Kolk**: Conceptualization (equal); Data curation (equal); Investigation (equal); Methodology (equal); Resources (equal); Writing – review & editing (equal). **Thomas Scholte**: Conceptualization (equal); Investigation (equal); Methodology (equal); Resources (equal); Software (equal); Validation (equal); Writing – review & editing (equal). **Harmen Smedes**: Data curation (equal); Formal analysis (equal); Investigation (equal); Methodology (equal); Resources (equal); Validation (equal); Writing – review & editing (equal). **R. Tufan Erdogan**: Data curation (equal); Investigation (equal); Methodology (equal); Resources (equal); Software (equal); Validation (equal); Writing – review & editing (equal). **Jin Chang**: Conceptualization (equal); Formal analysis (equal); Investigation (equal); Methodology (equal); Resources (equal); Supervision (equal); Validation (equal); Writing – review & editing (equal). **Hugo Voncken**: Data curation (equal); Formal analysis (equal); Software (equal); Validation (equal); Writing – review & editing (equal). **Jun Gao**: Conceptualization (equal); Funding acquisition (equal); Methodology (equal); Project administration (equal); Resources (equal); Supervision (equal); Writing – review & editing (equal). **Ali W Elshaari**: Funding acquisition (equal); Methodology (equal); Project administration (equal); Supervision (equal); Writing – review & editing (equal). **Simon Gröblacher**: Methodology (equal); Project administration (equal); Resources (equal); Supervision (equal). **Iman Esmaeil Zadeh**: Conceptualization (equal); Formal analysis (equal); Funding acquisition (equal); Investigation (equal); Methodology (equal); Project administration (equal); Resources (equal); Supervision (equal); Writing – review & editing (equal).

DATA AVAILABILITY

The data that support the findings of this study are available from the corresponding author upon reasonable request.

REFERENCES

[1] S. Shekhar, W. Bogaerts, L. Chrostowski, J. E. Bowers, M. Hochberg, R. Soref, and B. J. Shastri, "Roadmapping the next generation of silicon photonics," Nat. Commun. **15**, 751 (2024).
[2] K. Lu, Z. Chen, H. Chen, W. Zhou, Z. Zhang, H. K. Tsang, and Y. Tong, "Empowering high-dimensional optical fiber communications with integrated photonic processors," Nat. Commun. **15**, 3515 (2024).
[3] D. Pérez, I. Gasulla, P. Das Mahapatra, and J. Capmany, "Principles, fundamentals, and applications of programmable integrated photonics," Adv. Opt. Photonics **12**, 709–786 (2020).
[4] C. Yao, K. Xu, W. Zhang, M. Chen, Q. Cheng, and R. Penty, "Integrated reconstructive spectrometer with programmable photonic circuits," Nat. Commun. **14**, 6376 (2023).
[5] A. W. Elshaari, W. Pernice, K. Srinivasan, O. Benson, and V. Zwiller, "Hybrid integrated quantum photonic circuits," Nat. Photonics **14**, 285–298 (2020).
[6] E. Pelucchi, G. Fagas, I. Aharonovich, D. Englund, E. Figueroa, Q. Gong, H. Hannes, J. Liu, C.-Y. Lu, N. Matsuda *et al.*, "The potential and global outlook of integrated photonics for quantum technologies," Nat. Rev. Phys. **4**, 194–208 (2022).
[7] B. Jalali and S. Fathpour, "Silicon photonics," J. Lightwave Technol. **24**, 4600–4615 (2006).
[8] J. Komma, C. Schwarz, G. Hofmann, D. Heinert, and R. Nawrodt, "Thermo-optic coefficient of silicon at 1550 nm and cryogenic temperatures," Appl. Phys. Lett. **101**, 041905 (2012).
[9] H. H. Li, "Refractive index of silicon and germanium and its wavelength and temperature derivatives," J. Phys. Chem. Ref. Data **9**, 561–658 (1980).
[10] K. Johnson, N. Alshamrani, D. Almutairi, A. Grieco, C. Horvath, J. N. Westwood-Bachman, A. McKinlay, and Y. Fainman, "Determination of the nonlinear thermo-optic coefficient of silicon nitride and oxide using an effective index method," Opt. Express **30**, 46134–46146 (2022).
[11] A. D. Bristow, N. Rotenberg, and H. M. van Driel, "Two-photon absorption and Kerr coefficients of silicon for 850–2200 nm," Appl. Phys. Lett. **90**, 191104 (2007).

[12]H. K. Tsang, C. S. Wong, T. K. Liang, I. E. Day, S. W. Roberts, A. Harpin, J. Drake, and M. Asghari, "Optical dispersion, two-photon absorption and self-phase modulation in silicon waveguides at 1.5 μm wavelength," Appl. Phys. Lett. **80**, 416–418 (2002).
[13]V. Alex, S. Finkbeiner, and J. Weber, "Temperature dependence of the indirect energy gap in crystalline silicon," J. Appl. Phys. **79**, 6943–6946 (1996).
[14]R. Pässler, "Comparison of different analytical descriptions of the temperature dependence of the indirect energy gap in silicon," Solid-State Electron. **39**, 1311–1319 (1996).
[15]M. W. Puckett, K. Liu, N. Chauhan, Q. Zhao, N. Jin, H. Cheng, J. Wu, R. O. Behunin, P. T. Rakich, K. D. Nelson, and D. J. Blumenthal, "422 million intrinsic quality factor planar integrated all-waveguide resonator with sub-MHz linewidth," Nat. Commun. **12**, 934 (2021).
[16]J. Liu, G. Huang, R. N. Wang, J. He, A. S. Raja, T. Liu, N. J. Engelsen, and T. J. Kippenberg, "High-yield, wafer-scale fabrication of ultralow-loss, dispersion-engineered silicon nitride photonic circuits," Nat. Commun. **12**, 2236 (2021).
[17]N. Chauhan, J. Wang, D. Bose, K. Liu, R. L. Compton, C. Fertig, C. W. Hoyt, and D. J. Blumenthal, "Ultra-low loss visible light waveguides for integrated atomic, molecular, and quantum photonics," Opt. Express **30**, 6960–6969 (2022).
[18]M. Corato-Zanarella, X. Ji, A. Mohanty, and M. Lipson, "Absorption and scattering limits of silicon nitride integrated photonics in the visible spectrum," Opt. Express **32**, 5718–5728 (2024).
[19]M. Klanjšek Gunde and M. Maček, "Infrared optical constants and dielectric response functions of silicon nitride and oxynitride films," Phys. Status Solidi A **183**, 439–449 (2001).
[20]K. Ikeda, R. E. Saperstein, N. Alic, and Y. Fainman, "Thermal and Kerr nonlinear properties of plasma-deposited silicon nitride/silicon dioxide waveguides," Opt. Express **16**, 12987–12994 (2008).
[21]S. Kim, K. Han, C. Wang, J. A. Jaramillo-Villegas, X. Xue, C. Bao, Y. Xuan, D. E. Leaird, A. M. Weiner, and M. Qi, "Dispersion engineering and frequency comb generation in thin silicon nitride concentric microresonators," Nat. Commun. **8**, 372 (2017).
[22]A. Frigg, A. Boes, G. Ren, T. G. Nguyen, D.-Y. Choi, S. Gees, D. Moss, and A. Mitchell, "Optical frequency comb generation with low temperature reactive sputtered silicon nitride waveguides," APL Photonics **5**, 011302 (2020).
[23]J. W. Choi, B.-U. Sohn, G. F. R. Chen, D. K. T. Ng, and D. T. H. Tan, "Broadband incoherent four-wave mixing and 27 dB idler conversion efficiency using ultra-silicon rich nitride devices," Appl. Phys. Lett. **112**, 181101 (2018).
[24]Z. Yin, K. Sugiura, H. Takashima, R. Okamoto, F. Qiu, S. Yokoyama, and S. Takeuchi, "Frequency correlated photon generation at telecom band using silicon nitride ring cavities," Opt. Express **29**, 4821–4829 (2021).
[25]X. Zhu, C. Wang, B. E. Little, Z. Y. Ou, S. T. Chu, L. Cui, and X. Li, "Enhanced efficiency of correlated photon pairs generation in silicon nitride with a low-loss 3D edge coupler," APL Photonics **9**, 066102 (2024).
[26]C. Xiong, X. Zhang, A. Mahendra, J. He, D.-Y. Choi, C. J. Chae, D. Marpaung, A. Leinse, R. G. Heideman, M. Hoekman *et al.*, "Compact and reconfigurable silicon nitride time-bin entanglement circuit," Optica **2**, 724–727 (2015).
[27]L. Duan, T. J. Steiner, P. Pintus, L. Thiel, J. E. Castro, J. E. Bowers, and G. Moody, "Visible-telecom entangled-photon pair generation with integrated photonics: Guidelines and a materials comparison," ACS Photonics **12**, 118 (2024).
[28]X. Lu, Q. Li, D. A. Westly, G. Moille, A. Singh, V. Anant, and K. Srinivasan, "Chip-integrated visible–telecom entangled photon pair source for quantum communication," Nat. Phys. **15**, 373–381 (2019).
[29]M. J. R. Heck, J. F. Bauters, M. L. Davenport, D. T. Spencer, and J. E. Bowers, "Ultra-low loss waveguide platform and its integration with silicon photonics," Laser Photonics Rev. **8**, 667–686 (2014).
[30]J. F. Bauters, M. J. R. Heck, D. John, D. Dai, M.-C. Tien, J. S. Barton, A. Leinse, R. G. Heideman, D. J. Blumenthal, and J. E. Bowers, "Ultra-low-loss high-aspect-ratio Si_3N_4 waveguides," Opt. Express **19**, 3163–3174 (2011).
[31]T. A. Huffman, G. M. Brodnik, C. Pinho, S. Gundavarapu, D. Baney, and D. J. Blumenthal, "Integrated resonators in an ultralow loss Si_3N_4/SiO_2 platform for multifunction applications," IEEE J. Sel. Top. Quantum Electron. **24**, 5900209 (2018).
[32]M. B. Kleiner, S. A. Kuhn, and W. Weber, "Thermal conductivity measurements of thin silicon dioxide films in integrated circuits," IEEE Trans. Electron Devices **43**, 1602–1609 (1996).
[33]A. W. Elshaari, I. E. Zadeh, K. D. Jöns, and V. Zwiller, "Thermo-optic characterization of silicon nitride resonators for cryogenic photonic circuits," IEEE Photonics J. **8**, 2701009 (2016).
[34]A. Arbabi and L. L. Goddard, "Measurements of the refractive indices and thermo-optic coefficients of Si_3N_4 and SiO_x using microring resonances," Opt. Lett. **38**, 3878–3881 (2013).
[35]B. Lopez-Rodriguez, R. van der Kolk, S. Aggarwal, N. Sharma, Z. Li, D. van der Plaats, T. Scholte, J. Chang, S. Gröblacher, S. F. Pereira *et al.*, "High-quality amorphous silicon carbide for hybrid photonic integration deposited at a low temperature," ACS Photonics **10**, 3748–3754 (2023).
[36]B. Lopez-Rodriguez, N. Sharma, Z. Li, R. van der Kolk, J. van der Boom, T. Scholte, J. Chang, S. Gröblacher, and I. Esmaeil Zadeh, "Magic silicon dioxide for widely tunable photonic integrated circuits," ACS Photonics **12**, 1321 (2025).
[37]P. Xing, D. Ma, K. J. A. Ooi, J. W. Choi, A. M. Agarwal, and D. Tan, "CMOS-compatible PECVD silicon carbide platform for linear and nonlinear optics," ACS Photonics **6**, 1162–1167 (2019).
[38]P. Xing, D. Ma, L. C. Kimerling, A. M. Agarwal, and D. T. H. Tan, "High efficiency four wave mixing and optical bistability in amorphous silicon carbide ring resonators," APL Photonics **5**, 076110 (2020).
[39]Y. Lu, X. Shi, A. Ali Afridi, Y. Wang, V. Tabouret, D. Chaussende, K. Rottwitt, and H. Ou, "Strong third-order nonlinearity in amorphous silicon carbide waveguides," Opt. Lett. **49**, 4389–4392 (2024).
[40]L.-Y. S. Chang, H. Nejadriahi, S. Pappert, and P. K. L. Yu, "Demonstration of DC Kerr effect induced high nonlinear susceptibility in silicon rich amorphous silicon carbide," Appl. Phys. Lett. **120**, 071107 (2022).
[41]X. Lu, J. Y. Lee, S. Rogers, and Q. Lin, "Optical Kerr nonlinearity in a high-Q silicon carbide microresonator," Opt. Express **22**, 30826–30832 (2014).
[42]Z. Li, N. Sharma, B. Lopez-Rodriguez, R. van der Kolk, T. Scholte, H. Voncken, J. van der Boom, S. Gröblacher, and I. E. Zadeh, "Heterogeneous integration of amorphous silicon carbide on thin film lithium niobate," APL Photonics **10**, 016120 (2025).
[43]T. Alder, A. Stohr, R. Heinzelmann, and D. Jager, "High-efficiency fiber-to-chip coupling using low-loss tapered single-mode fiber," IEEE Photonics Technol. Lett. **12**, 1016–1018 (2000).
[44]R. Marchetti, C. Lacava, L. Carroll, K. Gradkowski, and P. Minzioni, "Coupling strategies for silicon photonics integrated chips [Invited]," Photonics Res. **7**, 201–239 (2019).
[45]R. Hauffe, U. Siebel, K. Petermann, R. Moosburger, J.-R. Kropp, and F. Arndt, "Methods for passive fiber chip coupling of integrated optical devices," IEEE Trans. Adv. Packag. **24**, 450–455 (2001).
[46]J. Fernández, R. Baños, D. Doménech, C. Domínguez, and P. Muñoz, "Low-loss inverted taper edge coupler in silicon nitride," IET Optoelectron. **13**, 62–66 (2019).
[47]M. Zhang, J. Wu, Z. Zhao, and K. Chen, "Efficient and polarization insensitive edge coupler based on cascaded vertical waveguide tapers," Opt. Express **31**, 31796–31805 (2023).
[48]G. Son, S. Han, J. Park, K. Kwon, and K. Yu, "High-efficiency broadband light coupling between optical fibers and photonic integrated circuits," Nanophotonics **7**, 1845–1864 (2018).
[49]X. Mu, S. Wu, L. Cheng, and H. Y. Fu, "Edge couplers in silicon photonic integrated circuits: A review," Appl. Sci. **10**, 1538 (2020).
[50]L. Cheng, S. Mao, Z. Li, Y. Han, and H. Fu, "Grating couplers on silicon photonics: Design principles, emerging trends and practical issues," Micromachines **11**, 666 (2020).
[51]T. Lin, H. Yang, L. Li, B. Yun, G. Hu, S. Li, W. Yu, X. Ma, X. Liang, and Y. Cui, "Ultra-broadband and highly efficient silicon nitride bi-layer grating couplers," Opt. Commun. **530**, 129209 (2023).
[52]R. Korček, P. Cheben, W. Fraser, J. H. Schmid, M. Milanizadeh, C. Alonso-Ramos, W. N. Ye, and D. Benedikovič, "Low-loss grating coupler based on inter-layer mode interference in a hybrid silicon nitride platform," Opt. Lett. **48**, 4017–4020 (2023).
[53]M. Kohli, D. Chelladurai, B. Vukovic, D. Moor, D. Bisang, K. Keller, A. Messner, T. Buriakova, M. Zervas, Y. Fedoryshyn *et al.*, "C- and O-band dual-polarization fiber-to-chip grating couplers for silicon nitride photonics," ACS Photonics **10**, 3366–3373 (2023).

[54]B. Chmielak, S. Suckow, J. Parra, V. C. Duarte, T. Mengual, M. A. Piqueras, A. L. Giesecke, M. C. Lemme, and P. Sanchis, "High-efficiency grating coupler for an ultralow-loss Si_3N_4-based platform," Opt. Lett. **47**, 2498–2501 (2022).
[55]Y. Xie, J. Wu, S. Hong, C. Wang, S. Liu, H. Li, X. Ju, X. Ke, D. Liu, and D. Dai, "Towards large-scale programmable silicon photonic chip for signal processing," Nanophotonics **13**, 2051–2073 (2024).
[56]Z. Xu, T. Zhou, M. Ma, C. Deng, Q. Dai, and L. Fang, "Large-scale photonic chiplet Taichi empowers 160-TOPS/W artificial general intelligence," Science **384**, 202–209 (2024).
[57]J. Bao, Z. Fu, T. Pramanik, J. Mao, Y. Chi, Y. Cao, C. Zhai, Y. Mao, T. Dai, X. Chen *et al.*, "Very-large-scale integrated quantum graph photonics," Nat. Photonics **17**, 573–581 (2023).
[58]Y. Wang, M. Chen, C. Yao, J. Ma, T. Yan, R. Penty, and Q. Cheng, "Asymmetrical estimator for training encapsulated deep photonic neural networks," Nat. Commun. **16**, 2143 (2025).
[59]X. Qiang, X. Zhou, J. Wang, C. M. Wilkes, T. Loke, S. O'Gara, L. Kling, G. D. Marshall, R. Santagati, T. C. Ralph *et al.*, "Large-scale silicon quantum photonics implementing arbitrary two-qubit processing," Nat. Photonics **12**, 534–539 (2018).
[60]S. R. Ahmed, R. Baghdadi, M. Bernadskiy, N. Bowman, R. Braid, J. Carr, C. Chen, P. Ciccarella, M. Cole, J. Cooke *et al.*, "Universal photonic artificial intelligence acceleration," Nature **640**, 368–374 (2025).
[61]X. Xu, G. Ren, T. Feleppa, X. Liu, A. Boes, A. Mitchell, and A. J. Lowery, "Self-calibrating programmable photonic integrated circuits," Nat. Photonics **16**, 595–602 (2022).
[62]W. Bogaerts, D. Pérez, J. Capmany, D. A. B. Miller, J. Poon, D. Englund, F. Morichetti, and A. Melloni, "Programmable photonic circuits," Nature **586**, 207–216 (2020).
[63]W. Luo, L. Cao, Y. Shi, L. Wan, H. Zhang, S. Li, G. Chen, Y. Li, S. Li, Y. Wang *et al.*, "Recent progress in quantum photonic chips for quantum communication and internet," Light: Sci. Appl. **12**, 175 (2023).
[64]L.-Y. S. Chang, S. Pappert, and P. K. L. Yu, "High thermo-optic tunability in PECVD silicon-rich amorphous silicon carbide," Opt. Lett. **48**, 1188–1191 (2023).
[65]Z. Li, B. Lopez-Rodriguez, N. Sharma, and I. Esmaeil-Zadeh, "Heterogeneous interconnection of low-loss and dense material platforms using adiabatic tapering coupler," EPJ Web Conf. **287**, 01014 (2023).
[66]N. Sharma, Z. Li, B. Lopez-Rodriguez, J. Vrugt, S. van der Waal, L. Li, R. van der Kolk, P. J. Poole, D. Dalacu, and I. Esmaeil Zadeh, "Design and validation of a-SiC/SiN hybrid photonic platform for integrated quantum photonics," Mater. Quantum Technol. **4**, 035401 (2024).
[67]L. Chrostowski and M. Hochberg, *Silicon Photonics Design: From Devices to Systems* (Cambridge University Press, 2015).
[68]F. Qiu, A. M. Spring, and S. Yokoyama, "Athermal and high-Q hybrid TiO_2–Si_3N_4 ring resonator via an etching-free fabrication technique," ACS Photonics **2**, 405–409 (2015).
[69]A. Chanana, H. Larocque, R. Moreira, J. Carolan, B. Guha, E. G. Melo, V. Anant, J. Song, D. Englund, D. J. Blumenthal *et al.*, "Ultra-low loss quantum photonic circuits integrated with single quantum emitters," Nat. Commun. **13**, 7693 (2022).
[70]Ł. Dusanowski, D. Köck, C. Schneider, and S. Höfling, "On-chip Hong–Ou–Mandel interference from separate quantum dot emitters in an integrated circuit," ACS Photonics **10**, 2941–2947 (2023).
[71]I. E. Zadeh, A. W. Elshaari, K. D. Jöns, A. Fognini, D. Dalacu, P. J. Poole, M. E. Reimer, and V. Zwiller, "Deterministic integration of single photon sources in silicon based photonic circuits," Nano Lett. **16**, 2289–2294 (2016).
[72]J. Chang, J. Gao, I. Esmaeil Zadeh, A. W. Elshaari, and V. Zwiller, "Nanowire-based integrated photonics for quantum information and quantum sensing," Nanophotonics **12**, 339–358 (2023).
[73]K. Mnaymneh, D. Dalacu, J. McKee, J. Lapointe, S. Haffouz, J. F. Weber, D. B. Northeast, P. J. Poole, G. C. Aers, and R. L. Williams, "On-chip integration of single photon sources via evanescent coupling of tapered nanowires to SiN waveguides," Adv. Quantum Technol. **3**, 1900021 (2020).
[74]S. Liu, J. Feng, Y. Tian, H. Zhao, L. Jin, B. Ouyang, J. Zhu, and J. Guo, "Thermo-optic phase shifters based on silicon-on-insulator platform: State-of-the-art and a review," Front. Optoelectron. **15**, 9 (2022).
[75]J. Parra, J. Navarro-Arenas, and P. Sanchis, "Silicon thermo-optic phase shifters: A review of configurations and optimization strategies," Adv. Photonics Nexus **3**, 044001 (2024).
[76]Y. Xie, Y. Shi, L. Liu, J. Wang, R. Priti, G. Zhang, O. Liboiron-Ladouceur, and D. Dai, "Thermally-reconfigurable silicon photonic devices and circuits," IEEE J. Sel. Top. Quantum Electron. **26**, 3600220 (2020).
[77]W. D. Sacher, Y. Huang, G.-Q. Lo, and J. K. S. Poon, "Multilayer silicon nitride-on-silicon integrated photonic platforms and devices," J. Lightwave Technol. **33**, 901–910 (2015).
[78]Z. Li, Z. Fan, J. Zhou, Q. Cong, X. Zeng, Y. Zhang, and L. Jia, "Process development of low-loss LPCVD silicon nitride waveguides on 8-inch wafer," Appl. Sci. **13**, 3660 (2023).
[79]D. B. Bonneville, J. W. Miller, C. Smyth, P. Mascher, and J. D. B. Bradley, "Low-temperature and low-pressure silicon nitride deposition by ECR-PECVD for optical waveguides," Appl. Sci. **11**, 2110 (2021).
[80]A. Frigg, A. Boes, G. Ren, I. Abdo, D.-Y. Choi, S. Gees, and A. Mitchell, "Low loss CMOS-compatible silicon nitride photonics utilizing reactive sputtered thin films," Opt. Express **27**, 37795–37805 (2019).
[81]H. Nejadriahi, S. Pappert, Y. Fainman, and P. Yu, "Efficient and compact thermo-optic phase shifter in silicon-rich silicon nitride," Opt. Lett. **46**, 4646–4649 (2021).
[82]N. A. Tyler, D. Fowler, S. Malhouitre, S. Garcia, P. Grosse, W. Rabaud, and B. Szelag, "Sin integrated optical phased arrays for two-dimensional beam steering at a single near-infrared wavelength," Opt. Express **27**, 5851–5858 (2019).
[83]M. Hai, A. Leinse, T. Veenstra, and O. Liboiron-Ladouceur, "A thermally tunable 1 × 4 channel wavelength demultiplexer designed on a low-loss Si_3N_4 waveguide platform," Photonics **2**, 1065–1080 (2015).
[84]D. T. Spencer, J. F. Bauters, M. J. R. Heck, and J. E. Bowers, "Integrated waveguide coupled Si_3N_4 resonators in the ultrahigh-*Q* regime," Optica **1**, 153–157 (2014).
[85]D. Bose, M. W. Harrington, A. Isichenko, K. Liu, J. Wang, N. Chauhan, Z. L. Newman, and D. J. Blumenthal, "Anneal-free ultra-low loss silicon nitride integrated photonics," Light: Sci. Appl. **13**, 156 (2024).